Enabling metal substrates for garnet-based composite cathodes by laser sintering

Walter Sebastian Scheld[1,2], Linda Charlotte Hoff[3], Christian Vedder[3,*], Jochen Stollenwerk[3], Daniel Grüner[4], Melanie Rosen[1], Sandra Lobe[1], Martin Ihrig[1], Ah-Ram Seok[1], Martin Finsterbusch[1,5], Sven Uhlenbruck[1,5], Olivier Guillon[1,5,6], Dina Fattakhova-Rohlfing[1,2,5,*]

[1] Forschungszentrum Jülich GmbH, Institute of Energy and Climate Research, Materials Synthesis and Processing IEK-1, 52425 Jülich, Germany

[2] University of Duisburg-Essen, Faculty of Engineering and Center for Nanointegration Duisburg-Essen CENIDE, Lotharstraße 1, 47057 Duisburg, Germany

[3] Fraunhofer Institute for Laser Technology ILT, Steinbachstr. 15, 52074 Aachen, Germany

[4] Forschungszentrum Jülich GmbH, Institute of Energy and Climate Research, Structure and Function of Materials IEK-2, 52425 Jülich, Germany

[5] Helmholtz Institute Münster: Ionics in Energy Storage IEK-12, Forschungszentrum Jülich GmbH, Corrensstr. 46, 48149 Münster, Germany

[6] Jülich Aachen Research Alliance: JARA-ENERGY, 52425 Jülich, Germany

* Corresponding author

christian.vedder@ilt.fraunhofer.de (Christian Vedder, Fraunhofer Institute for Laser Technology ILT, Steinbachstr. 15, 52074 Aachen, Germany)

d.fattakhova-rohlfing@fz-juelich.de (Dina Fattakhova-Rohlfing, Forschungszentrum Jülich GmbH, Institute of Energy and Climate Research, Materials Synthesis and Processing IEK-1, 52425 Jülich, Germany)

Keywords: laser sintering, composite cathode, screen-printing, LLZO, LCO, current collector, photonic sintering, garnet, $Li_7La_3Zr_2O_{12}$, $LiCoO_2$, solid-state battery

Abstract:

In this study, a laser irradiation method developed by Fraunhofer ILT was used to sinter screen-printed cathode layers of $LiCoO_2$ (LCO) and $Li_7La_3Zr_2O_{12}$ (LLZO) directly on a stainless steel current collector. The laser sintering method was proved to be a promising method to sinter the composite cathode onto steel with greatly reduced side reactions and material degradation. In comparison, conventional sintering and another light-absorption-based sintering method, namely rapid thermal processing (RTP) in a lamp furnace, led to almost complete decomposition of the LLZO phase accompanying with the detrimental formation of $LaCoO_3$ and CoO. Phase and morphology analysis of the laser-sintered cathodes using Raman spectroscopy, X-ray diffraction, and scanning electron microscopy confirmed sintering of LCO and LLZO through the layer with small amounts of secondary phases ($LaCoO_3$, $Li_{0.5}La_2Co_{0.5}O_4$ and CoO). The resulting porous matrix of the laser-sintered cathode was infiltrated with a polyethylene oxide (PEO) electrolyte to connect the cathode to an LLZO separator and a Li metal anode without an additional sintering step. This model cell was used to evaluate the electrochemical activity of the laser-sintered composite cathodes, which exhibited a specific discharge capacity of 102 mAh g^{-1} at 4.0 V in the first electrochemical cycle**.**

1. Introduction

Solid oxide Li-ion conductors are attracting much attention as electrolytes for all-solid-state batteries (ASB), which have great potential to outperform current liquid electrolyte batteries in terms of safety and energy density. A promising Li-ion conductor is the garnet-type

$Li_7La_3Zr_2O_{12}$ (LLZO) due to its room-temperature ionic conductivity up to ~1.5 mS cm^{-1}, its chemical stability with lithium metal, its processability in ambient atmosphere, its wide electrochemical stability window, and its non-flammability [1-6]. For the development of all-ceramic ASBs, LLZO should ideally not only act as a separator but also replace the conventional liquid electrolyte in the cathode layers by forming ceramic composite cathodes consisting of randomly distributed cathode active material (CAM) and LLZO [7]. Due to the ceramic nature of LLZO, a sintering step is required to bond the CAM and LLZO powders together and achieve the desired ionic and electronic conductivity of the composite cathode [8]. However, many CAMs decompose at elevated temperatures or react with the electrolyte to form detrimental secondary phases [9-12]. Among the various CAMs, $LiCoO_2$ (LCO) has the highest thermal stability against LLZO up to 1050 °C [13, 14]. Furthermore, LCO has a high specific capacity of 140 mAh g^{-1} and a high electronic conductivity of 1 mS cm^{-1}, which makes it a suitable CAM for garnet-based ASBs [15, 16].

To operate an ASB, both the cathode and the anode must be contacted with an electrically conductive metal foil, known as the current collector. In conventional Li-ion batteries with a liquid electrolyte, Cu and Al foils are used as current collectors. The electrode layers are deposited on the metal foils from a slurry containing organic binder molecules, which adheres well to the current collector and ensures good electrical contact without additional high-temperature annealing [17, 18]. In contrast, ceramic electrode layers have to be sintered. Therefore, an alternative cell design and processing in which the electrode layers (especially the cathode) are sintered directly onto the metal substrates that serve as current collectors or housing may be advantageous. However, sintering of the composite cathode on a metal substrate can lead to detrimental chemical reactions between them, the formation of insulating passivation layers on the current collector, or melting of the metal substrate

[19]. Therefore, the development of a sintering technique that selectively heats the cathode layer without excessively heating the current collector is of great interest for the future development of ceramic cell processing. One attractive technique in this field is laser sintering, which has become a successful commercial process for the selective sintering of numerous materials since it was first described in 1975 [20]. In laser sintering, a sample is moved under a laser beam with a low lateral spread and short interaction times. In this way, the heat generated by the absorption of the laser radiation (which depends on the optical properties of the material and the laser wavelength) is mainly transferred to the processed layer, while the underlying materials are not strongly affected, avoiding possible temperature-induced reactions with the substrate. This technique can be used to process different classes of material, e.g., polymers, metals, ceramics, or cermets with a variety of lasers such as excimer lasers (KrF, λ = 0.25 µm), Nd:YAG lasers (λ = 1.06 µm) or CO_2 lasers (λ = 10.60 µm) [21].

There have already been some attempts to process Li-containing battery materials by laser sintering, e.g., pure cathode materials such as $LiNi_{0.80}Co_{0.15}Al_{0.05}O_2$ (NCA) [22] and $LiMn_2O_4$ (LMO) [23] or $LiFePO_4$ (LFP) [24] incorporated into organic components. The $Li_{0.5}La_{0.5}TiO_3$ (LLTO) electrolyte has also been laser-sintered to achieve a high ionic conductivity of ~ 0.5 mS cm^{-1} [25]. Additionally, the laser sintering of garnet-based composite cathodes on steel substrates was recently published by some authors [26]. However, detailed study on the microstructure, phase analysis, and electrochemical performance of the cathode layer, which is important for the evaluation of the potential of the technology, was lacking.

To investigate the suitability of laser irradiation for selective sintering of ceramic composite cathodes on metal substrates and investigate their phase composition and electrochemical properties, the layers containing LCO and LLZO powders were screen printed on steel

substrates and then laser sintered [26]. The screen-printing technique is a scalable process that has already been used in the processing of ceramic layers, e.g., in the fabrication of solid oxide fuel cells [27, 28]. The stainless steel substrate acts as a current collector and provides the mechanical support for the ceramic layer. The introduction of steel substrates into the cell design has the potential to combine the current collector and cell housing into one, reducing the material cost for the current collector [17]. Finally, the sintered porous composite cathode was infiltrated with a polyethylene oxide (PEO) electrolyte to connect the cathode to an LLZO separator and a Li metal anode without an additional sintering step. This model cell was used to evaluate the electrochemical activity of the laser-sintered composite cathodes.

2. Experimental

2.1. Synthesis of LLZO

Ta- and Al-substituted LLZO ($Li_{6.45}Al_{0.05}La_3Zr_{1.6}Ta_{0.4}O_{12,}$ referred to hereafter as LLZO) powder was produced by a three-step solid-state reaction [29-31]. $LiOH{\cdot}H_2O$ (APPLICHEM, 99.00%), La_2O_3 (MERCK, 99.90%, pre-dried at 900 °C for 10 h), ZrO_2 (TREIBACHER, 99.70%), Ta_2O_5 (TREIBACHER, 99.99%), and Al_2O_3 (INFRAMAT, 99.82%) were dry-milled and then mixed stoichiometrically with an excess of 10 mol% $LiOH{\cdot}H_2O$. The resulting powder was pressed into pellets (45 mm in diameter, 19 MPa uniaxial pressure) and calcined in Al_2O_3 crucibles at 850 °C and 1000 °C for 20 h. Between the calcination steps, the powder was homogenized and pressed again into pellets. In the sintering step, 6 g pellets were pressed (13 mm in diameter, 113 MPa uniaxial pressure) and sintered in Al_2O_3 crucibles at 1175 °C with a dwell time of 10 h, using a MgO plate covered with an LLZO powder layer as a diffusion barrier. Some of the sintered pellets were sliced into thin discs for battery fabrication and the rest were ground for the fabrication of a screen-printing ink.

2.2. Cathode fabrication

The synthesized LLZO powder was mixed with commercial LCO powder (MTI CORPORATION) (50 wt% LCO : 50 wt% LLZO) and milled in 2-propanol (ALFA AESAR, 99.50%) in a planetary micro mill (PULVERISETTE 7, FRITSCH). The dispersion was dried in air at 50 °C and the resulting powder was mixed with a solution of 6 wt% ethyl cellulose (SIGMA-ALDRICH, 46 cps, 48.00%) in terpineol (SIGMA-ALDRICH, 99.50%). The slurry with a solid loading of 50 wt% was homogenized in a three-roll mill (50l, EXAKT) with a roll distance of 10 µm. It was printed on 2 mm thick steel substrates (THYSSENKRUPP SCHULTE GMBH, EN 1.4301) rinsed in ethanol (WERNER HOFMANN, 99.8%) by screen-printing (TISCHDRUCKGERAET HANKY TP 45, EICKMEYER GMBH) with a polyester screen (48-55×22.5°, KOENEN GMBH). The wet layers were dried in air at 35 °C for around 2 h. Afterwards, the ethyl cellulose which acts as a binder was removed in a separate pre-heating step in a conventional furnace in air with a heating rate of 2 K min^{-1} up to 500 °C with a dwell time of 30 min, followed by free cooling. The mass of the composite cathode was determined based on the difference in weight of the steel substrate before the screen-printing process and after the removal of the binder. The full cell had a diameter of 1.12 cm (A = 0.99 cm^2). The total mass of active material in the composite cathode was around 2.2 ± 0.2 mg (capacity: 0.31 ± 0.03 mAh). For comparative measurements, composite cathodes were printed on a 100 µm thick stainless steel substrate (EN 1.4767, VDM METALS) using the same deposition method described above. Subsequently, one part of the samples were processed in a conventional furnace with a heating rate of 10 K min^{-1} to 1050 °C for 30 min [13] and the other part was treated with rapid thermal processing (RTP) (XERION) with a gradual heating of 180 K min^{-1} with 10 second pauses in between to 1000 °C for 90 s like in [32].

2.3. Laser Sintering

For the laser sintering process, which was developed by Fraunhofer ILT [26], the samples were placed on a hot plate (FLE100640/TR400, BACH RESISTOR CERAMICS GMBH) pre-heated to 500 °C. The temperature of the hot plate surface near the sample was controlled with a thermocouple (GOF130 TYP K, GREISINGERELECTRONIC) and maintained 500 °C. The hot plate with the sample was located on a two-axis handling system (KREUZTISCH 10-V, ISEL GERMANY AG) for bidirectional moving with a feed velocity of 16 mm s^{-1} during the laser treatment in ambient atmosphere. Pre-heating is used to enhance the adhesion of the layer to the substrate during laser sintering, since low surface temperatures of the substrate tend to decrease the wetting of (partly) molten material and, thus, the adhesion [33, 34]. A laser (LIMO250-L6×0.07-DL1470-EX1682, LIMO GMBH) with a wavelength λ of 1470 nm, a maximum output power of 250 W, and line-shaped beam (6.3 mm × 0.084 mm) was used in continuous wave mode. The parameters for the laser sintering were chosen with respect to the sintering performance and phase stability of the cathode [26]. The laser power was set to 53.5 W, resulting in an interaction time of 5.3 ms and a power density of approx. 10.1 kW cm^{-2}, and the temperature at the laser focus can be assumed to be around 1000 °C to 1100 °C according to previous IR camera measurements [26]. After sintering, the samples were placed on a large metal plate at room temperature (RT) for cooling.

2.4. Battery assembly

The battery assembly was carried out in an Ar atmosphere. Polyethylene oxide (PEO) (SIGMA-ALDRICH, M_v = 600,000) was mixed with lithium bis(trifluoromethanesulfonyl)imide (LiTFSI) (SIGMA-ALDRICH, 99.95%) in a molar ratio of the repeat unit, ethylene oxide, to Li^+ of 20. Next, carbon black (ALFA AESAR, 99.99%) was added as an electronically conductive additive and all components were dissolved in acetonitrile (HONEYWELL, 99.8%). The laser-sintered composite cathodes were infiltrated by the prepared polymer solution and were dried for 1 h at 50 °C.

The sliced LLZO discs were polished with sandpaper and conditioned by an annealing step at 750 °C for 2 h in Ar. Metallic Li was pressed to obtain a thin foil, which was subsequently pressed onto the LLZO disc. The attached Li foil was then heated until it was molten to increase the contact between the anode and the electrolyte. This anodic half-cell was placed on the PEO composite cathode and the assembled full cell was placed in an ECC-REF cell housing (EL-CELL).

2.5. Characterization

X-ray diffraction (XRD) (D4 ENDEAVOR, BRUKER) was carried out in the Bragg-Brentano geometry with two-theta values of between 10° and 80° using Cu Kα radiation. Raman spectroscopy mapping (INVIA QONTOR, RENISHAW) was performed with a 532 nm laser (~5 mW) and a 2400 l mm^{-1} grating. The single spectra of the mapping were collected with an integration time of 1 s per spectrum and a step size of (x, y) = (1 µm, 1 µm) over an area of 80 µm × 40 µm, resulting in a total number of 3321 spectra. Cosmic ray removal, background subtraction, and normalization were applied to the spectra. Finally, LCO signals were extracted by a component analysis and the spectra for each phase were averaged. For top view scanning electron microscopy (SEM) (LEO 1455 EP, CARL ZEISS AG) analysis, a secondary electron (SE) detector was used, and the samples were coated with a thin Au layer prior to the analysis. Cross-sections were prepared by Ar-ion milling (SM-09010 CROSS-SECTION POLISHER, JEOL) for 6 h with an operating voltage of 6 kV. The microstructural analysis was performed using a field emission SEM (MERLIN, CARL ZEISS) with an accelerating voltage of 5 kV and a backscattered electron (BSE) detector. Energy dispersive X-ray spectroscopy (EDS) (X-MAX 80, OXFORD INSTRUMENTS) was performed with an accelerating voltage of 15 kV. The density of the cathodes was measured on the SEM images with the IMAGEJ software. The battery cell tests were performed in a climate chamber (VT 4002EMC,

VÖTSCH INDUSTRIETECHNIK) at 60 °C with a potentiostat (VMP-300, BIOLOGIC) with galvanostatic cycling with potential limitation (GCPL). The battery was charged in GCPL between 3 V and 4 V vs. Li with different currents depending on the C-rate, and the voltage was then kept at 4 V until the current declined to 1 µA.

3. Results and discussion

3.1. Laser sintering of LCO-LLZO cathode layers

The screen-printed composite cathode layers were pre-heated first to remove the organic binder molecules. The resulting flat black layers were analyzed by XRD, revealing only cubic LLZO (ICDD 99 000 0032) and rhombohedral LCO (ICDD 00 016 0427) phases after the pre-heating step (Figure 1A). After laser sintering (for more details check the earlier publication [26]), the cubic LLZO and rhombohedral LCO phases were present as the main phases. However, the formation of several secondary phases assigned to rhombohedral $LaCoO_3$ (ICDD 00 025 1060), cubic CoO (ICDD 01 071 1178) [35], and tetragonal $Li_{0.5}La_2Co_{0.5}O_4$ (ICDD 01 083 1842) [36] were detected.

To investigate whether the formation of secondary phases is due to the specifics of laser sintering (e.g., locally higher temperatures when irradiated with a laser beam compared to other sintering methods) or to a reaction with the steel substrate, the same cathode layers were sintered using both another light-absorption-based sintering method, namely sintering with a rapid thermal processing (RTP) lamp furnace, and conventional furnace sintering. The conventional furnace has slow heating rates and long dwell times so that the entire sample, including the steel substrate, is heated without temperature gradients in a processing time of hours. The RTP furnace has higher heating rates and short dwell times in the range of minutes, and heats only the surface of the cathode layer by absorption, creating a

temperature gradient during heating that is homogenized by heat conduction over the dwell time [20]. In laser sintering, the sample is heated at a moving position below the laser beam at extremely high heating rates with no dwell time, resulting in short interaction times in the range of milliseconds and producing much higher temperature gradients in the sample compared to other processes [20].

The optimal sintering parameters for RTP and conventional sintering of electrolyte-supported composite cathodes with complete phase retention have been described in previous publications [13, 32]. In this context, the LCO-LLZO system showed high thermal stability in electrolyte-supported cell designs at temperatures up to 1050 °C [9, 11, 13, 14]. The optimum sintering parameters [13, 32] were used to process composite cathodes by RTP and conventional sintering on the stainless steel substrate. This experiment was designed to evaluate the influence of the substrate on the stability of the composite cathodes during sintering.

XRD analysis of the steel-supported cathodes sintered with RTP and conventional sintering (Figure 1B) shows that the LLZO phase was completely decomposed, as indicated by the absence of the most intense LLZO reflection at 16.7°. $LaCoO_3$, $LiFeO_2$, $LiAl_2Cr_3O_8$ and $Al_{95}Fe_4Cr$ formed as secondary phases in the RTP process and $LaCoO_3$, $La_2Zr_2O_7$, and FeO in the conventional sintering process.

Since electrolyte supported LCO-LLZO composite cathodes sintered by RTP and conventional sintering [13, 32] as well as other sintering techniques [37-41] exhibit phase retention, this result indicates that the thermal stability of the composite cathodes are drastically lower when sintered on steel substrates. While the LLZO substrate [13, 32] likely serves as a Li reservoir, supporting the stability of the LCO-LLZO composite during sintering, the steel

substrate does not provide Li-ions. On the contrary, it may withdraw Li-ions from the composite cathode by reacting with the oxide layers which form on the steel surface during thermal processing [19]. In addition, undesirable reaction products are possible due to the diffusion of elements contained in the steel such as Fe, Cr, Al, Mn, or Ni.

Therefore, sintering of composite cathodes in a metal-supported cell design is much more challenging compared to electrolyte-supported cell designs. Laser sintering has been shown to be the only method for sintering LCO-LLZO composite cathodes on steel substrates that retains the LLZO phase. This is due to much shorter interaction times resulting in high temperature gradients, so that the steel substrate is less heated (selective sintering of the cathode) and consequently less oxidized and less reactive.

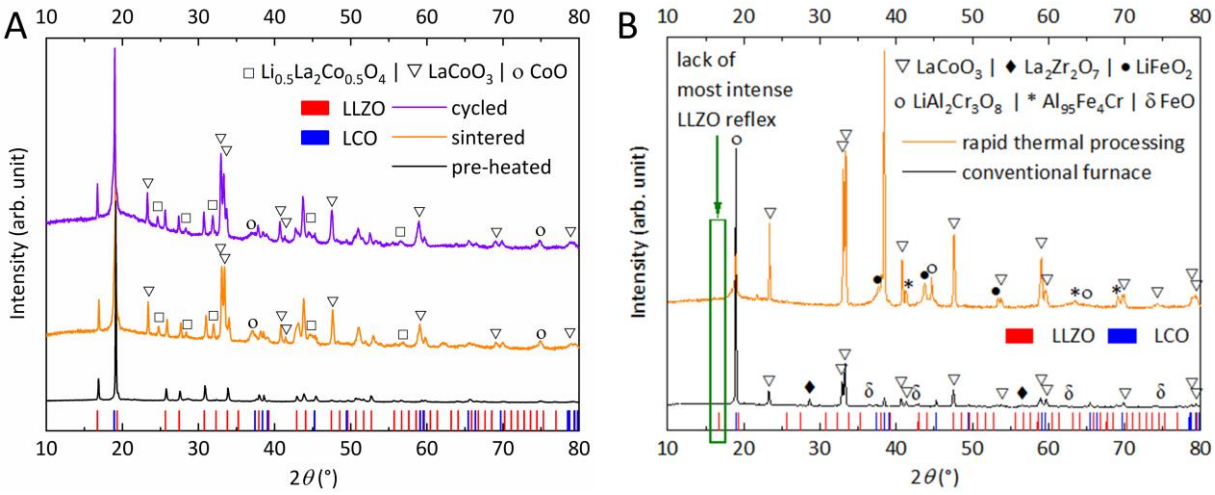

Figure 1: XRD measurements with respectively labeled major and minor phases. A) pre-heated composite cathode on steel with the laser-sintered and the electrochemically cycled cathode; B) sintered composite cathodes on EN 1.4767 steel substrates using a conventional furnace and rapid thermal processing with a insert hihglighting missing LLZO reflexes due to decomposition.

Raman spectroscopy was performed to obtain deeper insights into the phase composition of the LCO-LLZO composite cathode layers on the steel substrate after the different treatment steps, i.e. the pre-heating step, the laser sintering step, and the electrochemical cycling step (as described below). Evaluation of the individual phases in a typical Raman spectrum (Figure 2A) is difficult due to a strong superposition of the Raman signals. To deconvolute the

contribution of the LCO phase, its spectrum was extracted by component analysis (see Experimental part for more details) (Figure 2B). Due to the low intensity of the LLZO signals, extraction of the LLZO signals was not possible.

The E_g and A_{1g} LCO signals of the pre-heated, binder-removed sample show a shift to lower wavenumbers at 472 cm^{-1} and 583 cm^{-1} compared to the pristine rhombohedral LCO phase (space group $R\bar{3}m$), which has signals at 488 cm^{-1} and 597 cm^{-1} [42]. It is possible that preheating to 500 °C converted some of the LCO phase to the low-temperature cubic LCO phase (space group *Fd*3*m*), resulting in the strong shift to lower wavenumbers [43]. After laser sintering, the rhombohedral LCO phase appears to be restored, as indicated by LCO Raman signals at 484 cm^{-1} and 592 cm^{-1}. However, a 5 cm^{-1} shift to lower wavenumbers compared to the fully lithiated LCO phase (488 cm^{-1} and 597 cm^{-1} [42]) suggests that some amount of Li evaporated during sintering [44]. An additional signal at 684 cm^{-1} can be assigned to Co_3O_4, which was not detected by XRD measurements [45]. Since Raman spectroscopy is more surface sensitive than XRD, it is possible that Co_3O_4 formed at the surface of the cathode layer, while CoO was confirmed in deeper regions. In this context, it should be noted that direct heating during laser sintering of highly absorbing material, such as the LCO-LLZO composite cathode layers that have an absorbance of 73% at the laser wavelength of 1470 nm [26], mainly results in absorption of radiation in the upper parts of the cathode layer, while the underlying material is heated by thermal conduction. The energy transfer in deeper layers is thereby mainly influenced by the physical parameters of the specific heat capacity C_p ($C_{p(LLZO)}$ = 0.55 to 0.80 J g^{-1} K^{-1} [46], $C_{p(LCO)}$ = 0.73 J g^{-1} K^{-1} [47]) and heat conductivity k ($k_{(LLZO,\ RT\ to\ 900\ K)}$ = 1.45 to 1.55 W m^{-1} K^{-1} [46], $k_{(LCO)}$ = 5.4 W m^{-1} K^{-1} [48]), as well as the green density of the layer. Therefore, it is possible that the surface of the cathode layer reaches a higher temperature during laser sintering than the material in the

deeper parts of the cathode. The $LaCoO_3$ phase detected in the XRD measurements was not observed in the Raman spectra, which can most likely be explained by the different penetration depths and probe volumes of the two methods.

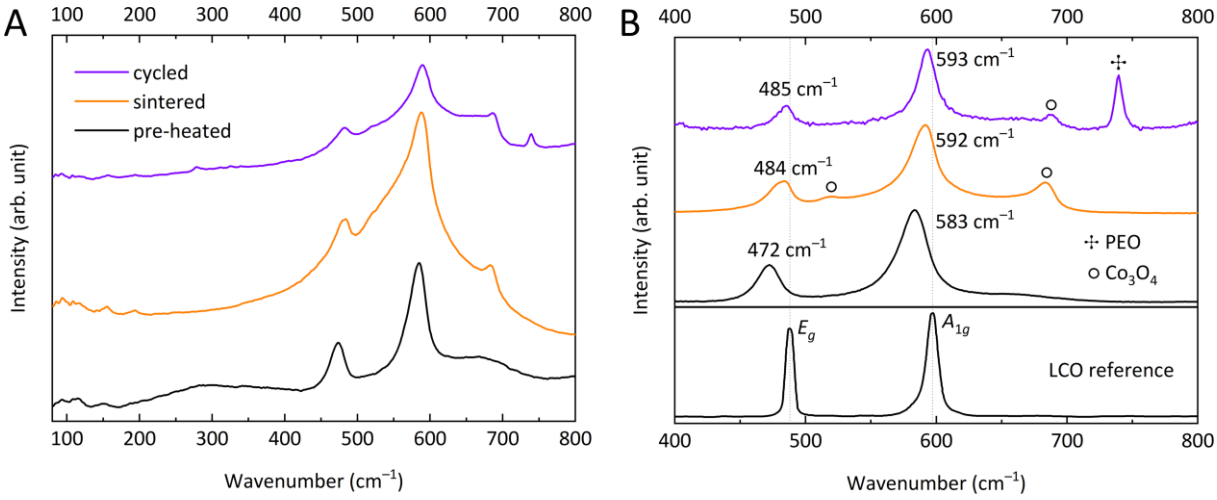

Figure 2: Raman spectroscopy measurements of the pre-heated, laser-sintered and electrochemically cycled composite cathode. A) average spectra of the Raman mapping; B) extracted LCO signals with wavenumbers of the signals, side phases and a pristine LCO reference spectrum with marked vibrational modes [42, 49].

Top view SEM images of the laser-sintered layers (Figure 3A-B) show the formation of a coherent structure with homogenously distributed macropores and a porosity of about 30%, as determined by digital analysis using ImageJ software. A cross-section of a polymer-infiltrated and electrochemically cycled composite cathode polished with Ar-ions shows sintering necks between the LCO and the LLZO particles, indicating that sintering was successful even in deeper regions (Figure 3C). However, the densification of the composite cathode during laser sintering is limited, as many pores can also be seen in the cross-section. In addition, the LCO, LLZO and secondary phases are inhomogeneously distributed in the layer. The relative density of the layer and homogenization of the phase distribution need to be improved for future optimization of electrode performance.

Based on the elemental contrast of the different materials and their mean atomic number $\bar{Z}$, the darker regions can be assigned to LCO, while the lighter regions correspond to LLZO. LCO

and LLZO are unevenly distributed over the layer thickness and the microstructure of the laser-sintered layer is not uniform. Regions with different microstructures can be distinguished. The areas labeled “1” in Figure 3C show well-sintered LCO-LLZO composite cathodes with low porosity and sintering necks between the particles. In addition to these regions, which closely resemble the targeted microstructure of co-sintered composite cathodes, much denser regions are also visible (labeled “2” in Figure 3C), consisting mainly of sintered LCO particles. The LLZO phase can be detected in these areas as light inclusions in the large LCO crystals. Since these areas are mainly located on the surface of the layers (“2”) that were directly exposed to the laser beam, it is very likely that they were formed as a result of the very rapid sintering. The growth of the LCO particles takes place at sites with a locally high temperature, which can be well above the sintering temperature of the LCO phase. LLZO particles do not form such large domains.

In addition to the dark LCO and light LLZO regions, some areas of intermediate gray-scale contrast were also detected (labeled “3”), probably corresponding to one of the detected cobalt-containing secondary phases such as $LaCoO_3$, $Li_{0.5}La_2Co_{0.5}O_4$, CoO, Co_3O_4, or a partially delithiated LCO. The latter three phases could be formed by the evaporation of Li from the LCO, which fits the results of the Raman spectroscopy analysis. The highest concentration of the secondary phases is visible at the surface of the laser-sintered layers, where they form separate domains (labeled “3”). These gray particles were also detected in regions consisting of small co-sintered LLZO and LCO particles (labeled “4”). This suggests that the secondary phases form preferentially in areas of high temperature, such as the surface directly exposed to laser radiation, and in areas with increased reactivity, such as small particles with a large interfacial area. Furthermore, some needle-like particles with light contrast were detected

(labeled “5”), which have not yet been identified and could correspond to one of the secondary phases.

The fact that sintering takes place even at quite deep levels is very encouraging and indicates that the heat supply via laser penetration depth and heat conduction is sufficient, rendering laser sintering a suitable method for densifying relatively thick composite cathode layers. It is also important to note that the steel substrate (labeled “6”) does not appear to be damaged by laser sintering or react with the cathode layer, as no oxide or secondary phase layers were detected on the steel|cathode interface. Considering the coefficients of thermal expansion (CTE) of EN 1.4301 steel with $1.8 \cdot 10^{-5}\ K^{-1}$ for 20 °C to 500 °C (according to the manufacturer), LCO with $1.3 \cdot 10^{-5}\ K^{-1}$ for 50 °C to 400 °C [50], and LLZO with $1.55 \cdot 10^{-5}\ K^{-1}$ for 25 °C to 700 °C [51], the question arises whether the mismatch of the CTEs of the different components can lead to cracking and delamination. In particular, LCO and the steel substrate exhibit large difference in CTEs. However, since laser processing produces a strong thermal gradient, the metal is heated less and the adverse effects of different CTEs during sintering are reduced [20]. This is also evident in the SEM cross-section, which shows good adhesion between the steel substrate and the cathode layer without large gaps or cracks at the interface. The black regions (labeled “7”) and the gray area on the top correspond to the polymer PEO (which was infiltrated after laser sintering). The PEO was used to connect the cathode to an LLZO separator and a Li metal anode without an additional sintering step. Some artifacts from the Ar-ion milling during the sample preparation for SEM can be seen labeled “8”, which originates from material being removed and deposited elsewhere.

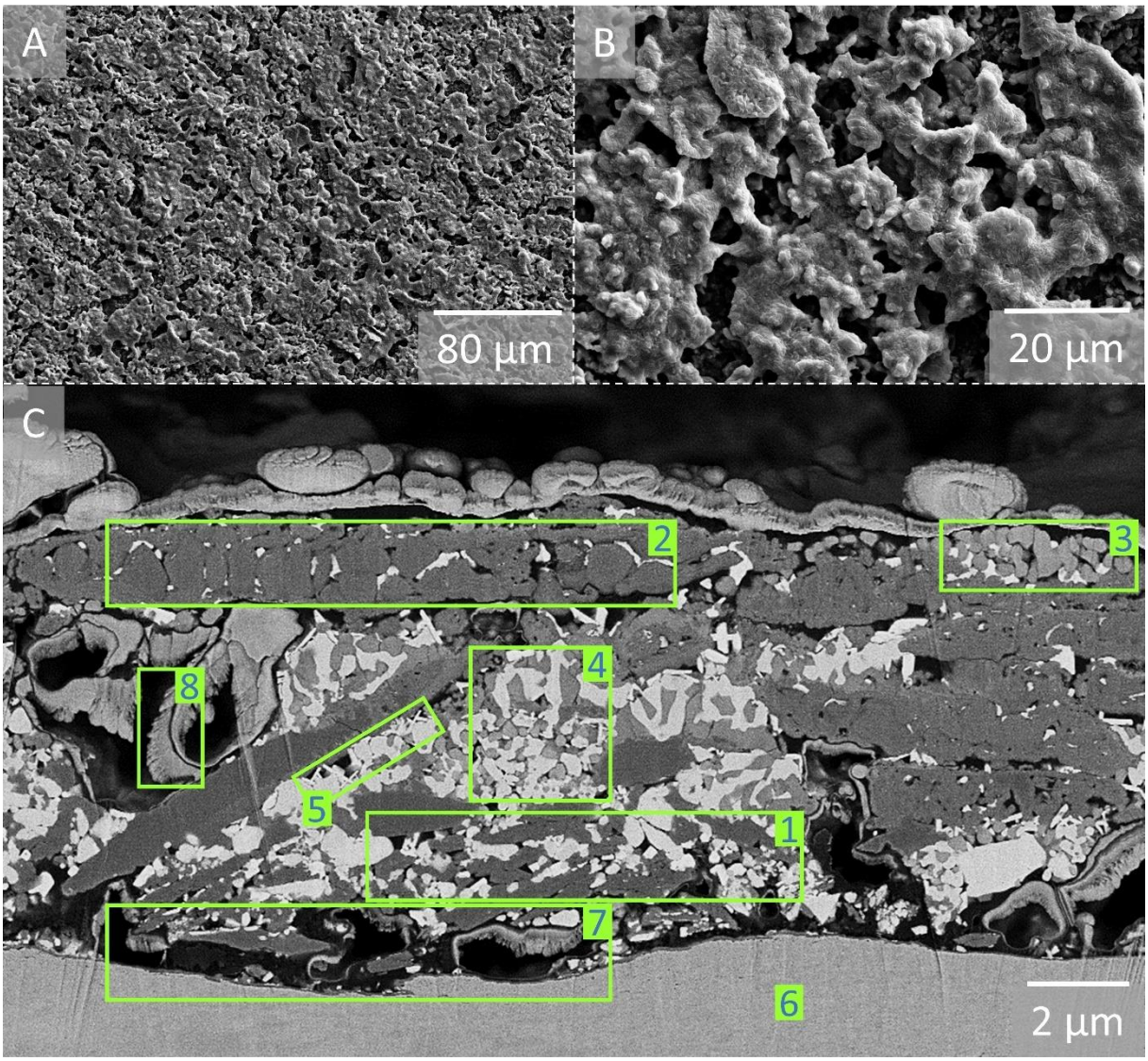

Figure 3: SEM images of the laser-sintered composite cathode. A) & B) top view images (SE) with different magnifications of the sintered cathode; C) cross-section view (BSE) of the PEO infiltrated and electrochemically cycled sample after Ar-ion milling. For details of the different highlighted areas, see the main text. During the Ar-ion milling process, material may be removed and deposited in other places, especially in pores ("8").

The element analysis of individual particles using EDS measurements (Figure 4A-B) confirms the presence of LLZO (spectrum 1) and LCO (spectrum 2) as the main phases. The detection of minor signals of Fe in both spectra can be explained by the previously mentioned deposited material from the Ar-ion milling, while the signals of La in the LCO spectrum (spectrum 2) can be assumed to be due to the excitation volume extending into the surrounding material. Since the Fe signals are present in both spectra (LLZO and LCO), the substitution of Fe into the LLZO lattice can probably be excluded and no evidence for any

other possible substitution in LLZO [52] was found. One of the regions with the gray contrast scale, which can be assumed to contain secondary phases, is measured in spectrum 3, where strong signals of Co, La, Zr, and O can be observed. It should be emphasized that these signals are probably influenced by the excitation volume, since the particles with the gray scale are much smaller than the LCO and LLZO particles. However, it is possible that $LaCoO_3$ and $Li_{0.5}La_2Co_{0.5}O_4$ formed right next to LLZO, which could explain the existence of the Co signal next to the LLZO particle. On the other hand, a Zr-rich phase must also form during decomposition of LLZO into La-Co phases. Such a phase was not detected by XRD and Raman spectroscopy and is still under investigation. The measurement performed on the PEO electrolyte (spectrum 4) shows a signal of S, corresponding to LiTFSI in the polymer electrolyte. The signals of other elements such as Fe, Cr, Ni, Si, and Mn originate from the steel substrate and those of Co and Zr from the composite cathode, as a result of the excitation volume extending into surrounding material. Spectrum 5 shows the elements of the steel substrate without any diffusion of La, Zr, or Co.

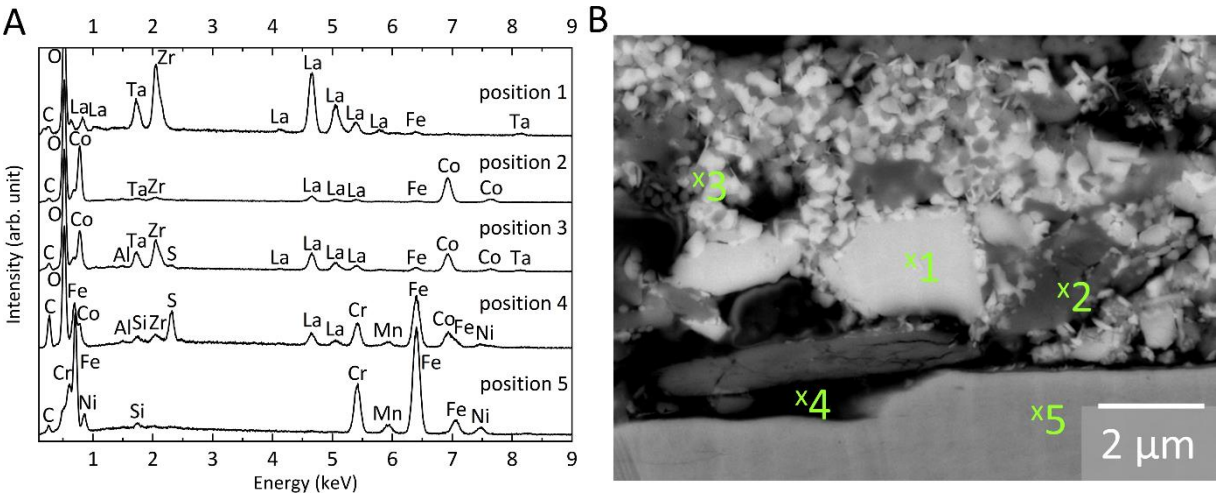

Figure 4: Cross sectional SEM image (BSE) with labeled EDS point measurements. A) EDS spectra from the different positions: (1) LLZO particle, (2) LCO particle, 3) area of secondary phases, 4) PEO, 5) steel substrate; B) SEM image.

To get a better idea of the diffusion of the elements in different regions, EDS mapping was performed in addition to point measurements (Figure 5). As expected, the lighter particles in

the BSE image, which are associated with the LLZO phase, show a light element contrast of La, Zr, Ta and O. In contrast, the darker particles in the BSE image of LCO show mainly Co and O, but La signals are also present. The La-EDS mapping indicates La-ion diffusion to the cathode particles, but at lower concentration than in LLZO particle. This result agrees well with the $LaCoO_3$ and $Li_{0.5}La_2Co_{0.5}O_4$ phases determined by XRD.

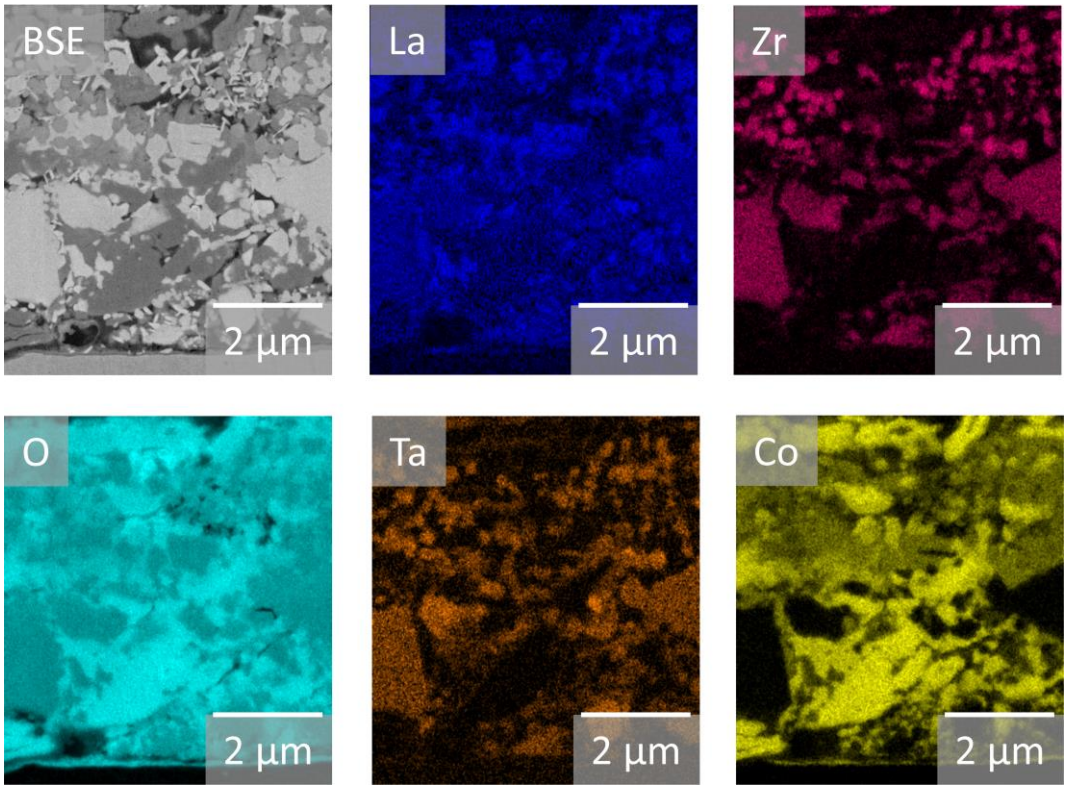

Figure 5: Cross sectional SEM image (BSE) with EDS mappings of La, Zr, O, Ta, and Co.

3.2. Electrochemical characterization

The electrochemical performance of the laser-sintered ceramic composite cathodes on the steel substrate was evaluated in a hybrid cell setup, which was previously used for ceramic composite cathodes by some of the authors of this study [53]. For this purpose, the porous cathode layer was infiltrated with the PEO polymer electrolyte, which was used to support ionic conductivity and to connect the cathode to an LLZO separator and a Li metal anode

without an additional sintering step (Figure 6A). Further optimization of the cell design would ultimately require sintering a ceramic separator onto the cathode so that PEO infiltration is no longer necessary. However, the cell design with PEO and LLZO pellets is suitable for the model cells in the current study for the purpose of evaluating the electrochemical performance of the laser-sintered composite cathodes.

In the cross-section image (Figure 3C) of the cathode, the infiltrated PEO can be seen in the open pores as material with black contrast (partially gray due to Ar-ion milling residues, see the area of Figure 3C labeled “8”). The infiltrated PEO can mainly be observed within the pores and on the surface of the composite cathode. Of particular note is the localization of PEO close to the steel substrate (labeled “7”), indicating successful infiltration.

The electrochemical activity of the laser-sintered and PEO-infiltrated composite cathode was characterized by galvanostatic charge/discharge with different current densities and C-rates (Figure 6B). In the first discharge cycle, a specific capacity of 102 mAh g^{-1} was achieved. Since the cathode was cycled only to 4.0 V, to prevent polymer electrolyte degradation at higher potentials, the cathode active material utilization is ~86% of the theoretical capacity of 118 mA g^{-1} (specific capacity of LCO charged/discharged at 4.2 V: 140 mAh g^{-1}) [16, 54].

In the subsequent cycles, a capacity fade was observed with a capacity loss of about ~5% per cycle. The capacity reduction was significantly increased by increasing the C-rate by about ~9% per cycle. This trend continued in the subsequent electrochemical cycles until finally, in the 12^{th} cycle, a specific discharge capacity of only 54 mAh g^{-1} was reached, corresponding to a capacity fade of 47%. The individual discharge capacities and the respective coulombic efficiency are summarized in Figure 6C, which illustrates the increased capacity loss for the different C-rates and shows a decreased coulombic efficiency, especially in the first

electrochemical cycles with a higher C-rate. Overall, the coulombic efficiency increases with a higher number of electrochemical cycles.

The XRD patterns (Figure 1A) and Raman spectra (Figure 2B) of the electrochemically cycled layer are practically indistinguishable from those of the as-prepared layers. They show no signs of phase change induced by the electrochemical cycling, indicating no strong degradation of the crystal phase after electrochemically cycling (a signal was observed at 740 cm^{-1} which can be assigned to the PEO electrolyte [55]). Therefore, the observed capacity fading could be due to the phase transformation in a very thin interfacial layer, as described in a previous study on LCO-LLZO cathodes by Ihrig et al. [37]. However, it should be noted that the observed capacity fade of the laser-sintered LCO-LLZO cathode on the steel substrate is comparable to electrolyte supported LCO-LLZO based cathodes processed by other sintering techniques [13, 32, 37-41, 56]. This suggests the cause of the observed capacity fade as the intrinsic electrochemical instability of unprotected LCO-LLZO composite cathodes and not by the laser sintering process [37]. In comparison, electrolyte supported and conventional sintered LCO-LLZO based batteries showed capacity retentions after electrochemical cycling between 30% to 72% (30% [13], 42% [8], 50% [57], 72% [58]), while cells processed with SPS or FAST/SPS showed capacity retentions of 60% [59] and 64% [38]. Hot-pressed cells lead to a capacity retention of 64% [60] and ultra-fast high-temperature sintering (UHS) to a value of 69% [61]. The cathodes presented in the study are in the middle range with a capacity retention of 53%, which demonstrates that the laser-sintered cathode does not result to increased electrochemical degradation.

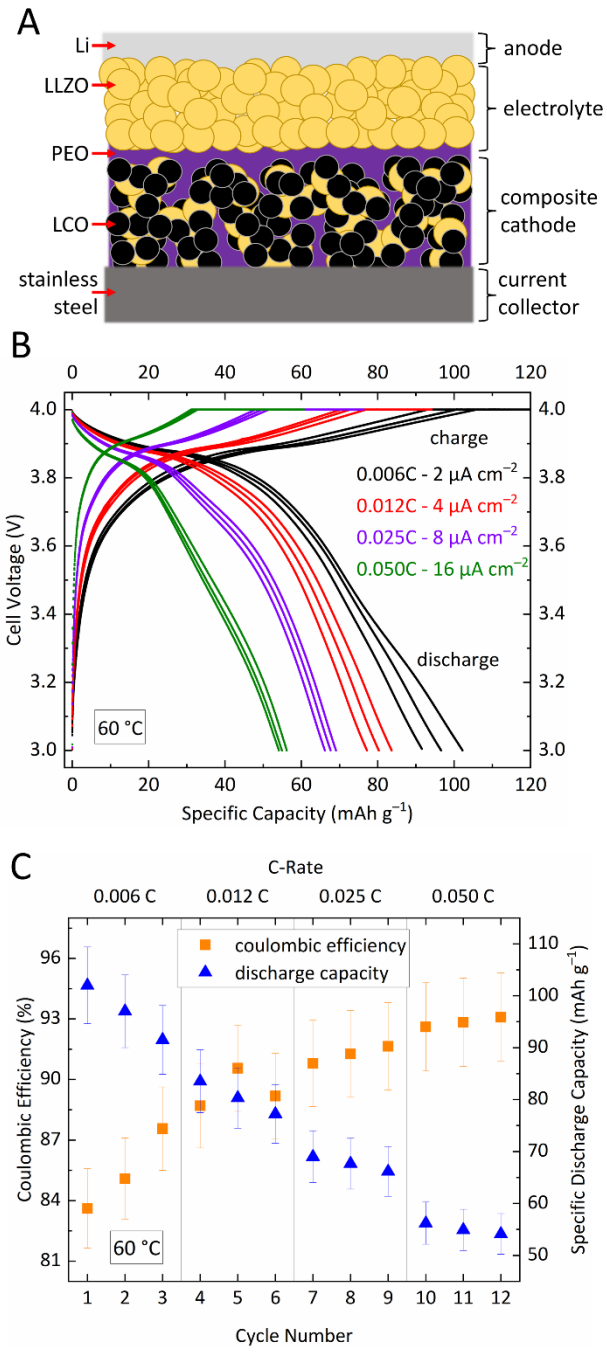

Figure 6: Electrochemical measurements of the cell. A) scheme of the manufactured battery with descriptions of the individual components; B) GCPL measurements of the polymer infiltrated battery at 60 °C, progressing from small C-rates and current densities to larger ones; C) the coulombic efficiency with the discharge capacity of the individual electrochemical cycles shown with the different C-rates.

4. **Conclusion**

LCO-LLZO based composite cathodes were screen-printed on stainless steel substrates and sintered by a laser irradiation method [26]. The sintered material showed phase retention of LLZO and LCO on the steel substrate with a La-ion diffusion into the LCO particles leading to small amounts of $LaCoO_3$, $Li_{0.5}La_2Co_{0.5}O_4$, and CoO secondary phases. In comparison, conventional sintering, and rapid thermal processing (RTP) in a lamp furnace resulted in almost complete decomposition of the LLZO phase. A model cell with PEO, LLZO and metallic Li allowed electrochemical battery testing. The laser-sintered cathode layers showed a high specific capacity of 102 mAh g^{-1} while cycling at 4.0 V (86% cathode utilization) in the first discharge cycle and for LCO-LLZO cells typical moderate capacity retention of 53% after 12 electrochemical cycles.

The experimental results demonstrate the suitability of laser sintering for the densification of ceramic composite cathode layers on thermally reactive metallic substrates. Based on our own experiments and literature research, no other sintering process has demonstrated the ability to sinter ceramic composite cathodes directly on a metal substrate. If the parent LLZO and LCO phases could be further preserved and the La-Co secondary phases avoided, even better battery performance would likely be conceivable. In addition, the homogeneity of the LCO and LLZO phases must be further increased. If LLZO layers can also be sintered on at sufficient density, it is conceivable that it will be possible to manufacture all-ceramic half-cells with significantly thinner layer thicknesses and shorter production times.

Declaration of Competing Interest

The authors declare no conflict of interest.

Acknowledgment

This work was funded by the German Federal Ministry for Economic Affairs and Climate Action (BMWK) within the OptiKeraLyt project (grant no. 03ETE016F), as well as by the German Federal Ministry of Education and Research (BMBF) as part of the FestBatt2-Oxide (grant no. 13XP0434A) and CatSE (grant no. 13XP0223A) projects. The authors would like to thank VDM Metals for providing the EN 1.4767 steel.

Received: ((will be filled in by the editorial staff))

Revised: ((will be filled in by the editorial staff))

Published online: ((will be filled in by the editorial staff))

References

[1] Wang C, Fu K, Kammampata SP, McOwen DW, Samson AJ, Zhang L, et al. Garnet-Type Solid-State Electrolytes: Materials, Interfaces, and Batteries. Chem Rev. 2020;120:4257-300.
[2] Janek J, Zeier WG. A solid future for battery development. Nat Energy. 2016;1.
[3] Murugan R, Thangadurai V, Weppner W. Fast lithium ion conduction in garnet-type Li(7)La(3)Zr(2)O(12). Angew Chem Int Ed. 2007;46:7778-81.
[4] Thompson T, Yu S, Williams L, Schmidt RD, Garcia-Mendez R, Wolfenstine J, et al. Electrochemical Window of the Li-Ion Solid Electrolyte Li7La3Zr2O12. ACS Energy Lett. 2017;2:462-8.
[5] Wu JF, Chen EY, Yu Y, Liu L, Wu Y, Pang WK, et al. Gallium-Doped Li7La3Zr2O12 Garnet-Type Electrolytes with High Lithium-Ion Conductivity. ACS Appl Mater Interfaces. 2017;9:1542-52.
[6] Ihrig M, Mishra TP, Scheld WS, Häuschen G, Rheinheimer W, Bram M, et al. Li7La3Zr2O12 solid electrolyte sintered by the ultrafast high-temperature method. Journal of the European Ceramic Society. 2021;41:6075-9.
[7] Kim KJ, Rupp JLM. All ceramic cathode composite design and manufacturing towards low interfacial resistance for garnet-based solid-state lithium batteries. Energy Environ Sci. 2020;13:4930-45.
[8] Finsterbusch M, Danner T, Tsai CL, Uhlenbruck S, Latz A, Guillon O. High Capacity Garnet-Based All-Solid-State Lithium Batteries: Fabrication and 3D-Microstructure Resolved Modeling. ACS Appl Mater Interfaces. 2018;10:22329-39.

[9] Miara L, Windmuller A, Tsai CL, Richards WD, Ma Q, Uhlenbruck S, et al. About the Compatibility between High Voltage Spinel Cathode Materials and Solid Oxide Electrolytes as a Function of Temperature. ACS Appl Mater Interfaces. 2016;8:26842-50.
[10] Ren Y, Liu T, Shen Y, Lin Y, Nan C-W. Chemical compatibility between garnet-like solid state electrolyte Li6.75La3Zr1.75Ta0.25O12 and major commercial lithium battery cathode materials. J Materiomics. 2016;2:256-64.
[11] Wakasugi J, Munakata H, Kanamura K. Thermal Stability of Various Cathode Materials against Li_{6.25}Al_{0.25}La₃Zr₂O₁₂ Electrolyte. J Electrochem Soc Jpn. 2017;85:77-81.
[12] Zhang N, Long X, Wang Z, Yu P, Han F, Fu J, et al. Mechanism Study on the Interfacial Stability of a Lithium Garnet-Type Oxide Electrolyte against Cathode Materials. ACS Appl Energy Mater. 2018;1:5968-76.
[13] Tsai C-L, Ma Q, Dellen C, Lobe S, Vondahlen F, Windmüller A, et al. A garnet structure-based all-solid-state Li battery without interface modification: resolving incompatibility issues on positive electrodes. Sustain Energy Fuels. 2019;3:280-91.
[14] Uhlenbruck S, Dornseiffer J, Lobe S, Dellen C, Tsai C-L, Gotzen B, et al. Cathode-electrolyte material interactions during manufacturing of inorganic solid-state lithium batteries. J Electroceramics. 2016;38:197-206.
[15] Tukamoto H, West AR. Electronic Conductivity of LiCoO2 and Its Enhancement by Magnesium Doping. J Electrochem Soc. 2019;144:3164-8.
[16] Mizushima K, Jones PC, Wiseman PJ, Goodenough JB. LixCoO 2 (0<x~l): A NEW CATHODE MATERIAL FOR BATTERIES OF HIGH ENERGY DENSITY. Mater Res Bull. 1980;15:783-9.
[17] Whitehead AH, Schreiber M. Current Collectors for Positive Electrodes of Lithium-Based Batteries. J Electrochem Soc. 2005;152.
[18] Sousa RE, Oliveira J, Gören A, Miranda D, Silva MM, Hilliou L, et al. High performance screen printable lithium-ion battery cathode ink based on C-LiFePO4. Electrochimica Acta. 2016;196:92-100.
[19] Scheld WS, Lobe S, Uhlenbruck S, Dellen C, Sohn YJ, Hoff LC, et al. Rapid thermal sintering of screen-printed LiCoO2 films. Thin Solid Films. 2022;749:139177.
[20] Rebohle L, Prucnal S, Skorupa W. A review of thermal processing in the subsecond range: semiconductors and beyond. Semiconductor Science and Technology. 2016;31.
[21] Kruth JP, Wang X, Laoui T, Froyen L. Lasers and materials in selective laser sintering. Assembly Automation. 2003;23:357-71.
[22] Acord KA, Dupuy AD, Scipioni Bertoli U, Zheng B, West WC, Chen QN, et al. Morphology, microstructure, and phase states in selective laser sintered lithium ion battery cathodes. Journal of Materials Processing Technology. 2021;288.
[23] Chen X, Sastre J, Rumpel M, Flegler A, Singhania A, Balta Bonner J, et al. Photonic methods for rapid crystallization of LiMn2O4 cathodes for solid-state thin-film batteries. J Power Sources. 2021;495.
[24] Phillips T, Milroy C, Beaman J. Creating Conformable Lithium Batteries Using Selective Laser Sintering. Proceedings of the 32nd Annual International Solid Freeform Fabrication Symposium – An Additive Manufacturing Conference. Austin, Texas, USA 2021. p. 702 - 13.
[25] Silva JHL, Alves YGS, Almeida A, Agostinho Moreira J, Vilarinho R, Santos JCA, et al. Study of the ionic conductivity of Li0.5La0.5TiO3 laser-sintered ceramics. Journal of the European Ceramic Society. 2020;40:5619-25.
[26] Hoff LC, Scheld WS, Vedder C, Stollenwerk J. Laser sintering of ceramic-based solid-state battery materials. Laser-based Micro- and Nanoprocessing XVI. San Francisco, Californica, United States2022.
[27] Baharuddin NA, Abdul Rahman NF, Abd. Rahman H, Somalu MR, Azmi MA, Raharjo J. Fabrication of high-quality electrode films for solid oxide fuel cell by screen printing: A review on important processing parameters. International Journal of Energy Research. 2020;44:8296-313.
[28] Jia C, Ma Q, Han M, Wang W, Menzler NH, Guillon O. Fabrication and Performance of La, Co-Substituted SrTiO3 as Cathode Materials of Solid Oxide Fuel Cell. ECS Transactions. 2019;91:1291.

[29] Mann M, Küpers M, Häuschen G, Finsterbusch M, Fattakhova-Rohlfing D, Guillon O. The influence of hafnium impurities on the electrochemical performance of tantalum substituted Li7La3Zr2O12 solid electrolytes. Ionics. 2021;28:53-62.
[30] Mann M, Kupers M, Hauschen G, Finsterbusch M, Fattakhova-Rohlfing D, Guillon O. Evaluation of Scalable Synthesis Methods for Aluminum-Substituted Li7La3Zr2O12 Solid Electrolytes. Materials. 2021;14.
[31] Tsai C-L, Dashjav E, Hammer E-M, Finsterbusch M, Tietz F, Uhlenbruck S, et al. High conductivity of mixed phase Al-substituted Li7La3Zr2O12. J Electroceramics. 2015;35:25-32.
[32] Scheld WS, Lobe S, Dellen C, Ihrig M, Hauschen G, Hoff LC, et al. Rapid thermal processing of garnet-based composite cathodes. J Power Sources. 2022;545:231872.
[33] Vedder C, Wollgarten S, Gradmann R, Stollenwerk J, Wissenbach K, Eberstein M. Laser-based functionalization of electronic multi-material-layers for embedded sensors. Journal of Laser Applications. 2017;29:226031–7.
[34] Sändker H. Laserbasierte Herstellung funktionaler Beschichtungen aus partikulärem Polyetheretherketon. Aachen: RWTH Aachen University, Lehrstuhl für Technologie Optischer Systeme TOS; 2019.
[35] Jung DH, Umirov N, Kim T, Bakenov Z, Kim JS, Kim SS. Thermal and Structural Stabilities of LixCoO2 Cathode for Li Secondary Battery Studied by a Temperature Programmed Reduction. Eurasian Chem-Technol J. 2019;21:3-12.
[36] Ghosh P, Mahanty S, Basu RN. Lanthanum-doped LiCoO2 cathode with high rate capability. Electrochimica Acta. 2009;54:1654-61.
[37] Ihrig M, Finsterbusch M, Laptev AM, Tu CH, Tran NTT, Lin CA, et al. Study of LiCoO2/Li7La3Zr2O12:Ta Interface Degradation in All-Solid-State Lithium Batteries. ACS Appl Mater Interfaces. 2022;14:11288-99.
[38] Ihrig M, Finsterbusch M, Tsai C-L, Laptev AM, Tu C-h, Bram M, et al. Low temperature sintering of fully inorganic all-solid-state batteries – Impact of interfaces on full cell performance. J Power Sources. 2021;482.
[39] Sastre J, Chen X, Aribia A, Tiwari AN, Romanyuk YE. Fast Charge Transfer across the Li7La3Zr2O12 Solid Electrolyte/LiCoO2 Cathode Interface Enabled by an Interphase-Engineered All-Thin-Film Architecture. ACS Appl Mater Interfaces. 2020;12:36196-207.
[40] Park K, Yu B-C, Jung J-W, Li Y, Zhou W, Gao H, et al. Electrochemical Nature of the Cathode Interface for a Solid-State Lithium-Ion Battery: Interface between LiCoO2 and Garnet-Li7La3Zr2O12. Chem Mater. 2016;28:8051-9.
[41] Ihrig M, Ye R, Laptev AM, Grüner D, Guerdelli R, Scheld WS, et al. Polymer–Ceramic Composite Cathode with Enhanced Storage Capacity Manufactured by Field-Assisted Sintering and Infiltration. ACS Appl Energy Mater. 2021;4:10428-32.
[42] Freitas BGA, Siqueira JM, da Costa LM, Ferreira GB, Resende JALC. Synthesis and Characterization of LiCoO2 from Different Precursors by Sol-Gel Method. J Braz Chem Soc. 2017;28:2254-66.
[43] Huang W, Frech R. Vibrational spectroscopic and electrochemical studies of the low and high temperature phases of LiCo, _xM,O, (M = Ni or Ti). Solid State Ionics. 1996;86-88:395-400.
[44] Nishi T, Nakai H, Kita A. Visualization of the State-of-Charge Distribution in a LiCoO2Cathode by In Situ Raman Imaging. J Electrochem Soc. 2013;160:A1785-A8.
[45] Rivas-Murias B, Salgueiriño V. Thermodynamic CoO-Co3O4 crossover using Raman spectroscopy in magnetic octahedron-shaped nanocrystals. J Raman Spectrosc. 2017;48:837-41.
[46] Neises J, Scheld WS, Seok A-R, Lobe S, Finsterbusch M, Uhlenbruck S, et al. Study of thermal material properties for Ta- and Al-substituted Li7La3Zr2O12 (LLZO) solid-state electrolyte in dependency of temperature and grain size. J Mater Chem A. 2022;10:12177-86.
[47] H. K, Takematsu M, Tojo T, Atake T, Hirano A, Kanno R. Low temperature heat capacity and thermodynamic functions of LiCoO2. Journal of Thermal Analysis and Calorimetry. 2002;68:833-9.
[48] Cho J, Losego MD, Zhang HG, Kim H, Zuo J, Petrov I, et al. Electrochemically tunable thermal conductivity of lithium cobalt oxide. Nat Commun. 2014;5:4035.

[49] Gross T, Hess C. Raman diagnostics of LiCoO2 electrodes for lithium-ion batteries. J Power Sources. 2014;256:220-5.
[50] Cheng EJ, Taylor NJ, Wolfenstine J, Sakamoto J. Elastic properties of lithium cobalt oxide (LiCoO2). Journal of Asian Ceramic Societies. 2018;5:113-7.
[51] Hubaud AA, Schroeder DJ, Ingram BJ, Okasinski JS, Vaughey JT. Thermal expansion in the garnet-type solid electrolyte (Li7−Al/3)La3Zr2O12 as a function of Al content. Journal of Alloys and Compounds. 2015;644:804-7.
[52] Miara LJ, Richards WD, Wang YE, Ceder G. First-Principles Studies on Cation Dopants and Electrolyte|Cathode Interphases for Lithium Garnets. Chem Mater. 2015;27:4040-7.
[53] Rosen M, Finsterbusch M, Guillon O, Fattakhova-Rohlfing D. Free standing dual phase cathode tapes – scalable fabrication and microstructure optimization of garnet-based ceramic cathodes. J Mater Chem A. 2022;10:2320-6.
[54] Carlier D, Croguennec L, Ceder G, Menetrier M, Shao-Horn Y, Delmas C. Structural study of the T#2-LixCoO2 (0.52 < x < or = 0.72) phase. Inorg Chem. 2004;43:914-22.
[55] Rey I, Lassègues JC, Grondin J, Servant L. Infrared and Raman study of the PEO-LiTFSI polymer electrolyte. Electrochimica Acta. 1998;43:1505-10.
[56] Ihrig M, Kuo LY, Lobe S, Laptev AM, Lin CA, Tu CH, et al. Thermal Recovery of the Electrochemically Degraded LiCoO(2)/Li(7)La(3)Zr(2)O(12):Al,Ta Interface in an All-Solid-State Lithium Battery. ACS Appl Mater Interfaces. 2023;15:4101-12.
[57] Ramkumar B, So-young K, Chan-woo N, Aravindan V, Yun-Sung L. LiBO2-modified LiCoO2 as an efficient cathode with garnet framework Li6.75La3Zr1.75Nb0.25O12 electrolyte toward building all-solid-state lithium battery for high-temperature operation. Electrochimica Acta. 2020;359.
[58] Ren Y, Liu T, Shen Y, Lin Y, Nan Y-W. Ionics. 2017;23:2521-7.
[59] Zheng C, Tang S, Wen F, Peng J, Yang W, Lv Z, et al. Reinforced cathode-garnet interface for high-capacity all-solid-state batteries. Mater Futures. 2022;1.
[60] Feng W, Lai Z, Dong X, Li P, Wang Y, Xia Y. Garnet-Based All-Ceramic Lithium Battery Enabled by Li(2.985)B(0.005)OCl Solder. iScience. 2020;23:101071.
[61] Ping W, Wang C, Wang R, Dong Q, Lin Z, Brozena AH, et al. Printable, high-performance solid-state electrolyte films. Sci Adv. 2020;6.